Where Quantum and Fluids entangle

Quantum Computational Fluid Dynamics
Core Gate Level QCFD Set
Project number 101080085

Call:	HORIZON-CL4-2021-DIGITAL-EMERGING-02
Topic:	HORIZON-CL4-2021-DIGITAL-EMERGING-02-10
Type of action:	HORIZON Research and Innovation Actions
Granting authority:	European Commission-EU
Project starting date: fixed date:	1 November 2022
Project end date:	31 October 2026
EU-Project duration:	48 months
Project Coordinator:	University of Hamburg (UHH)
Work Package Leader	Forschungszentrum Juelich (FZJ)
Cooperations	Technical University of Crete (TUC), University of Hamburg (UHH)
Deliverable number:	D6.1
WP contributing to the deliverable:	WP#6 Gate Level Simulations
Deliverable Type:	Data
Revision:	0
Dissemination level:	Public
Due Submission date:	31.10.2024
Prepared By:	FZJ, TUC
Internal Reviewers:	DJ, DA, MK
Final Approval:	DJ

This project receives funding from the European Union's Horizon 2020 HORIZON Research and Innovation Actions Programme under Grant Agreement #101080085

Revision History

Version	Date	Who	Changes
R0	15.10.2024	FM	

1 Executive Summary

The Quantum Computational Fluid Dynamics (QCFD) project is dedicated to establishing an open-access quantum software framework to address Computational Fluid Dynamics (CFD) challenges present in today's industry.

As a part of the Work Package 6 (WP6) ”Gate-Level simulations”, Deliverable D6.1 provides a core set of “small benchmark” examples of solutions computed with quantum circuit gate-level simulations. These problems are simplified to be able to run on current and short term capabilities of quantum computers, and provide a basis for comparison with benchmark CFD solutions from work packages 1 and 4.

In accordance with the Data Management Plan (DMP), D6.1 follows the FAIR data principles – Findability, Accessibility, Interoperability, and Reusability – where each dataset is provided with a detailed metadata structure with unique identifiers and proper documentation, ensuring that the data is not only easily accessible but also readily transferable and reusable. The access to the public is granted by a dedicated research data repository (FDR) hosted at the university of Hamburg (UHH), https://www.fdr.uni-hamburg.de/communities/qcfd/. To facilitate the users overview, all datasets belonging to the QCFD project, namely those from this report (which include 10.25592/uhhfdm.14123, 10.25592/uhhfdm.16129, 10.25592/uhhfdm.16108, and 10.25592/uhhfdm.16108), are collected in a QCFD community group on the mentioned data server.

Contents

1 Executive Summary **3**

2 Introduction **5**

3 Platforms **5**

4 Gate-level implementation **7**

5 Data Organization **8**

6 Nonlinear Schroedinger equation **8**
- 6.1 Hadamard test measurement error: 9
- 6.2 Benchmarking Simulations in Ideal Settings: 10
- 6.3 Simulations Incorporating Superconducting Quantum Hardware Noise 11

7 Heat Equation **12**
- 7.1 Benchmarking Simulations in Ideal Settings 13
- 7.2 Benchmarking Simulations with limited statistics 14
- 7.3 Benchmarking Simulations with Noise Models 15

8 Burgers Equation **16**
- 8.1 Benchmarking Simulations in Ideal Settingss 17
- 8.2 Benchmarking Simulations with limited statistics 18
- 8.3 Benchmarking Simulations with Noise Model Statistics 19

2 Introduction

Solving numerically differential equations is at the heart of science and engineering because many fundamental processes in nature are described by such equations. Examples include the convection-diffusion process, wave dynamics, fluid dynamics to name a few [1]. The typical approach for solving these equations is to discretize the solution candidate in position and time and write the derivatives (variations) using approximate methods such as finite difference and solve the differential equation iteratively [2]. The main problem with this approach relies on the increasing number of resources for simulating these systems up to a bounded precision, requiring high-parallelization and high-performance computing.

Therefore new computational technologies are required. One possible approach relies on using quantum computers, where it has been proposed that solving algorithms on them may lead to better asymptotic scaling, when compared with its classical counterpart [3, 4]. In this framework, we can exploit the elements from gate-based quantum computation for encoding the required operations (time and spatial derivative) and variational quantum circuits [5] for engineering adequate candidates (anzätzes) of the solution. Both problems (operation and anzatz) are mapped to quantum circuits that can be run on an operative quantum computer. Nowadays, there are a wide range of potential quantum computers running with a modest number of qubits in the so-called Noise Intermediate-Scale Quantum Computers (NISQ) [6] from different platform such as photons [7], neutral atoms [8], trapped-ions [9] and superconducting circuits [10, 11]. Each of them has its own strengths and disadvantages that can exploited to solve differential equations. For this deliverable, we explore the possibility to encode a set of differential equations - namely the Schroedinger Non Linear equation, the Heat equation and the Burgers' equation - on quantum computers based on Trapped-Ions represented by Quantinuum® simulators and on superconducting circuit architectures, modeled by IBM quantum simulators, for different initial conditions.

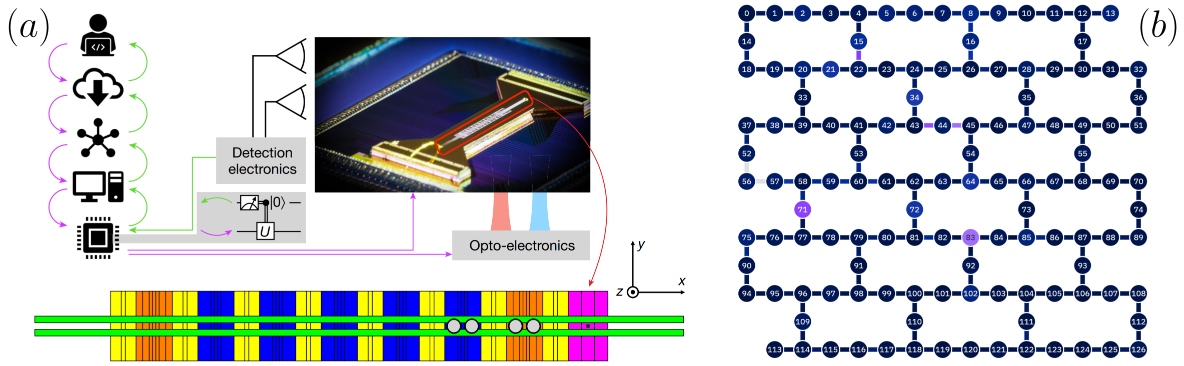

Figure 1: Representation of a Trapped Ion Computer (a) from [12] and an IBM 127 superconducting qubits quantum Computers(b) from [11]. As mentioned, whilst the Ion trap allows for all-to-all connectivity, the superconducting computer possesses a limited topology, where only certain connections between qubits are allowed.

3 Platforms

We discuss the gatesets and models for the two platforms above that are examined in this report.

We used a model of Quantinuum H1 series, that consist of twenty $^{114}\mathrm{Yb}^{+}$ ions [see Fig. 1(a)], as the a representative of Ion Traps. The platform uses optical lasers for addressing individual or pairs of these ions to implement single- two-qubit gates. Moreover, it is possible to address different pairs of ions so that a two qubit gate can be established between any qubit - it implements *all-to-all* connectivity [12]. Single-qubit gates are generated by resonant lasers [13], whereas the two-qubit gates are implemented through the quantized movement of the ions in the interaction zones [14]. Finally, the readout is performed by shining the system and measuring the fluorescence spectrum [15]. The native set of gates available in the processor are the following:

- Single-qubit gates

$$U_{1\mathrm{q}}(\theta,\phi)=\begin{pmatrix}\cos\frac{\theta}{2} & -ie^{-i\phi}\sin\frac{\theta}{2}\\ -ie^{i\phi}\sin\frac{\theta}{2} & \cos\frac{\theta}{2}\end{pmatrix},\quad R_z(\lambda)=\begin{pmatrix}e^{-i\frac{\lambda}{2}} & 0\\ 0 & e^{i\frac{\lambda}{2}}\end{pmatrix},\tag{1}$$

- Two-qubit gate

$$\mathrm{ZZ} = \begin{pmatrix} 1 & 0 & 0 & 0 \\ 0 & i & 0 & 0 \\ 0 & 0 & i & 0 \\ 0 & 0 & 0 & 1 \end{pmatrix}, \quad \mathrm{RZZ}(\theta) = \begin{pmatrix} 1 & 0 & 0 & 0 \\ 0 & e^{i\theta} & 0 & 0 \\ 0 & 0 & e^{i\theta} & 0 \\ 0 & 0 & 0 & 1 \end{pmatrix}, \tag{2}$$

- General SU(4) entangler

$$R(\alpha,\beta,\gamma) = \begin{pmatrix} e^{-i\frac{\gamma}{2}}\cos\left(\frac{\alpha-\beta}{2}\right) & 0 & 0 & e^{i\frac{\gamma}{2}}\cos\left(\frac{\alpha+\beta}{2}\right) \\ 0 & -ie^{-i\frac{\gamma}{2}}\sin\left(\frac{\alpha-\beta}{2}\right) & -ie^{i\frac{\gamma}{2}}\sin\left(\frac{\alpha+\beta}{2}\right) & 0 \\ 0 & -ie^{i\frac{\gamma}{2}}\sin\left(\frac{\alpha+\beta}{2}\right) & -ie^{-i\frac{\gamma}{2}}\sin\left(\frac{\alpha-\beta}{2}\right) & 0 \\ e^{i\frac{\gamma}{2}}\cos\left(\frac{\alpha+\beta}{2}\right) & 0 & 0 & e^{-i\frac{\gamma}{2}}\cos\left(\frac{\alpha-\beta}{2}\right) \end{pmatrix}. \tag{3}$$

System Fundamentals	**min**	**typ**	**max**
Qubits	20	20	20
Connectivity	All-to-all		
Parallel two-qubit operations	5	5	5
Errors			
Single-qubit gate	1×10^{-5}	2×10^{-5}	2×10^{-4}
Two-qubit gate	8×10^{-4}	1×10^{-3}	3×10^{-3}
State preparation and measurement	2×10^{-3}	3×10^{-3}	5×10^{-3}

Table 1: Specification of the H1 Quantinuum processor.

As expected, the implementation of all these operations together with the readout process are affected by the unavoidable action of the environment, leading to gate and readout errors summarized in Table 1.

On the other hand, we have analysed the simulated performances of the IBM superconducting quantum processors `Sherbrooke`. The processor consist of 127 Transmon qubits [16] capacitively connected to auxiliary resonators on a grid configuration [dark blue lines on Fig. 1(b)]. Unlike the Quantinuum processor, the IBM architecture does not support *all-to-all* connectivity. Instead, for performing operation between distant qubits swap operations are needed, increasing the overhead of the circuit. In this architecture, both single- and two-qubit operations are implemented by voltage-controlled microwave drives addressing one [17] or both qubit at the same time [18, 19]. Finally, the readout of the qubit is performed using an auxiliary resonator so that the measured voltage is proportional to the state of the qubit [20, 21]. For these architectures, the native set of gates are the following

- Single-qubit gates

$$\sqrt{X} = \frac{1}{2}\begin{pmatrix} 1+i & 1-i \\ 1-i & 1+i \end{pmatrix}, \quad X = \begin{pmatrix} 0 & 1 \\ 1 & 0 \end{pmatrix}, \quad \mathrm{RZ}(\lambda) = \begin{pmatrix} e^{-i\frac{\lambda}{2}} & 0 \\ 0 & e^{i\frac{\lambda}{2}} \end{pmatrix}. \tag{4}$$

- Two-qubit gates

$$\mathrm{ECR} = \frac{1}{\sqrt{2}}\begin{pmatrix} 0 & 0 & 1 & i \\ 0 & 0 & i & 1 \\ 1 & -i & 0 & 0 \\ -i & 1 & 0 & 0 \end{pmatrix} \tag{5}$$

Similar to the Trapped-ion cases, all these operations are affected by the action of the electronic environment that introduces relaxation, decoherence and crosstalk [22]. The typical errors affecting the architecture are summarized on Table 2.

Qubit	**Readout**	**ID**	$\sqrt{X}$	**Pauli-X**	**ECR**
0	4.80	2.008	2.008	2.008	1_0:0.0134
1	2.13	3.565	3.565	3.565	1_2:0.0095
2	5.40	2.633	2.633	2.633	1_0:0.0134
3	1.30	2.214	2.214	2.214	3_2:0.0089
4	1.72	1.618	1.618	1.618	4_3:0.0046
5	4.61	2.933	2.933	2.933	5_4:0.0072

Table 2: Error source of the Sherbrooke IBM quantum processor.

4 Gate-level implementation

The idea of this project is to use variational quantum circuits for encoding the solution ansatz and the operations needed for solving partial differential equations (PDE) on one of the aforementioned quantum processors. We focus on diffusion and fluid dynamics problems governed by the Heat and the Navier-Stokes equations, respectively, following the approach developed in Ref. [23] where they propose the variational quantum circuit depicted in Fig. 2(a) for encoding the velocity field in the amplitudes of a multi-qubit wave function. Moreover, the gradients, Laplacian and non-linear terms present on the Navier-Stoke equation are encoded in multi-controlled quantum gates as depicted in Fig. 2(b) so that each terms of the differential equation are obtained by measuring a *master qubit* and then optimized to find the optimal variational parameters. Thus, we aim to decompose these interactions in terms of the native set available on each quantum processor and compare the advantages/disadvantages for solving the PDE more efficiently.

The fundamental problem that we may face is the *transpilation* i.e, how do we decompose the quantum circuit into the native gate set whilst respecting the connectivity of the quantum processor. In this case, Quantinuum has the advantages that it is possible to implement all-to-all quantum gates, decreasing the required number of two-qubit gates making the decomposition shorter. Moreover, the fidelity of these quantum gates is higher in comparison with its superconducting circuit counterpart. Nevertheless, the gate time of these quantum gates are longer than in superconducting qubits (μs vs ns) which limits the number of single-shoot measurements before the decoherence destroy completely the quantum state. On the other hand, as we have pointed out, superconducting quantum processors are able to implement faster single- and two-qubit gates, but they are more noisy than in traped-ions and present limited connectivity [see Fig. 1(b)] so that for implementing multi-controlled operation in an all-to-all fashion, we require a large number of swap operations that limits the fidelity for the encoding of the solution as well as the implementation of the finite difference operations. One strength of superconducting processors over the trapped-ion processor is the larger maximal number of single-shoot measurement, which allows us to achieve better convergence and even make possible to implement noise mitigation techniques such as zero noise extrapolation (ZNE) [25]. Thus, for having a better understanding of the detrimental effect present on the quantum processors, we will perform numerical simulations without and with noise models to later show the performance of the variational algorithm on real quantum processors.

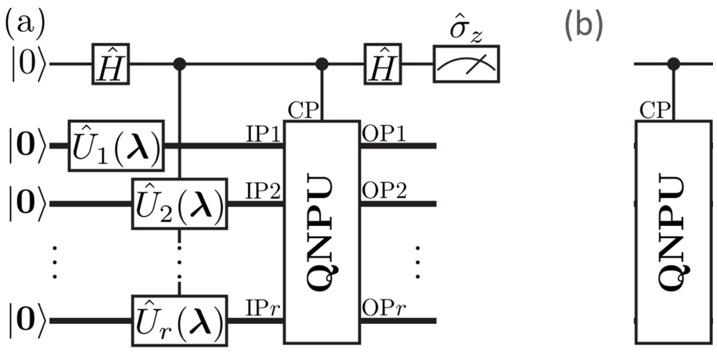

Figure 2: Variational algorithm to solve non linear problems such as fluid dynamics simulations from [24]. b) - multi-controlled gates necessary for the algorithm

5 Data Organization

Following the model of previous reports, we maintain the same guidelines for data accuracy and transparency. Therefore, for each equation analysed we provide the parameters and field obtained at each time step in easily readable files either in *.txt* format or *.npy* format. All data is clearly labeled and indicated in the appropriate file. All numbers are used with double-precision floating-point number format.

To access the data obtained throughout this report we mainly used 2 criteria: **Fidelity** - the similarity measure and formed by the scalar product of two normalized vectors - and the **Mean Squared Error** - an average measure of the squared difference between 2 data sets.

6 Nonlinear Schroedinger equation

The nonlinear Schrödinger equation (NLSE) and its variants model various phenomena [26, 27, 28, 29, 30, 31, 32, 33, 34, 35], such as dynamics of light in nonlinear optics [28, 29], envelope solitons and modulation instabilities in plasma physics and surface gravity waves [30], and characteristics including superfluidity and vortex formation in Bose-Einstein Condensates (BEC) [31, 32, 33, 34, 35], to name a few. In dimensionless form, the time-independent NLSE is given as

$$\Big[-\frac{1}{2}\frac{d^2}{dx^2}+V(x)+gI_{f(x)}\Big]f(x)=Ef(x)\ . \qquad (6)$$

Here, $f(x)$, with x being spatial coordinates, represents a normalized single real-valued function defined over the interval $[a,b]$. The term $I_{f(x)}$ represents the nonlinear interaction, g denotes the strength of the nonlinearity, and $V(x)$ is the external potential. In this study, we consider $I_{f(x)} = |f(x)|^2$, quadratic potential $V(x) = V_0(x-x_0)^2$ centered around $x_0 = \frac{b-a}{2}$, and periodic boundary conditions such that $f(b) = f(a)$ and $V(b) = V(a)$. Small instances of the Eq. (6) can be solved numerically on classical computers by employing imaginary-time evolution [36, 33, 37], spectral, variational or other methods [26]. However, when addressing large instances of nonlinear problems, the limitations associated with memory capacity and computational time inherent in classical computation become increasingly apparent.

Following standard numerical approaches, we discretize the interval $[a,b]$ into N equidistant points $x_k = a+\delta k$, where $\delta = (b-a)/N$ is the spacing between two adjacent grid points, and $k \in \{0,1,2,\dots,N-1\}$. The normalization condition on the function $f(x)$ takes the form $1 = \delta\sum_{k=0}^{N-1}|f(x_k)|^2 = \sum_{k=0}^{N-1}|\psi_k|^2$, where we have defined $\psi_k = \sqrt{\delta}f(x_k)$. We encode the $N = 2^n$ amplitudes ψ_k, which may also incorporate the initial conditions of the problem, into the basis states $|\text{binary}(k)\rangle$ of the n-qubit quantum register such that the quantum state takes the form $|\Psi\rangle = \sum_k \psi_k|\text{binary}(k)\rangle$. By applying the finite-difference method, the expectation value of the total energy [from Eq. (6)] of the system is given as the sum of potential, interaction, and kinetic

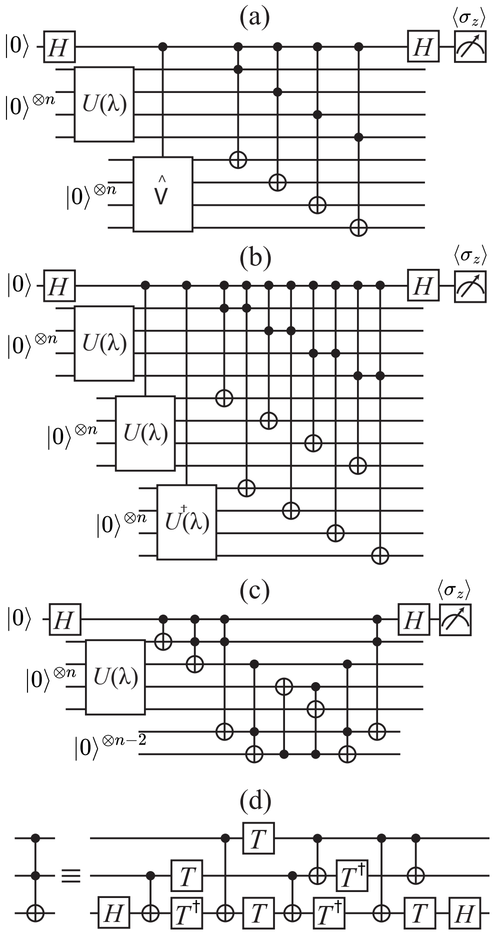

Figure 3: Design of the quantum circuits used to measure the (a) potential, (b) interaction, and (c) kinetic energies. Here, H is the Hadamard gate, $U(\lambda)$ is the quantum ansatz that represents the trial state, and $\hat{V}$ is the potential unitary which encodes the potential function values to the basis states. Here, we have shown an example of $n = 4$ $(n' = 13)$, which can be generalized to an arbitrary number of qubits. Panel (d) shows the decomposition of the Toffoli gate into a sequence of single-qubit gates and controlled-NOT gates, where $T = R_z(\pi/4)$ and $T^{\dagger} = R_z(-\pi/4)$.

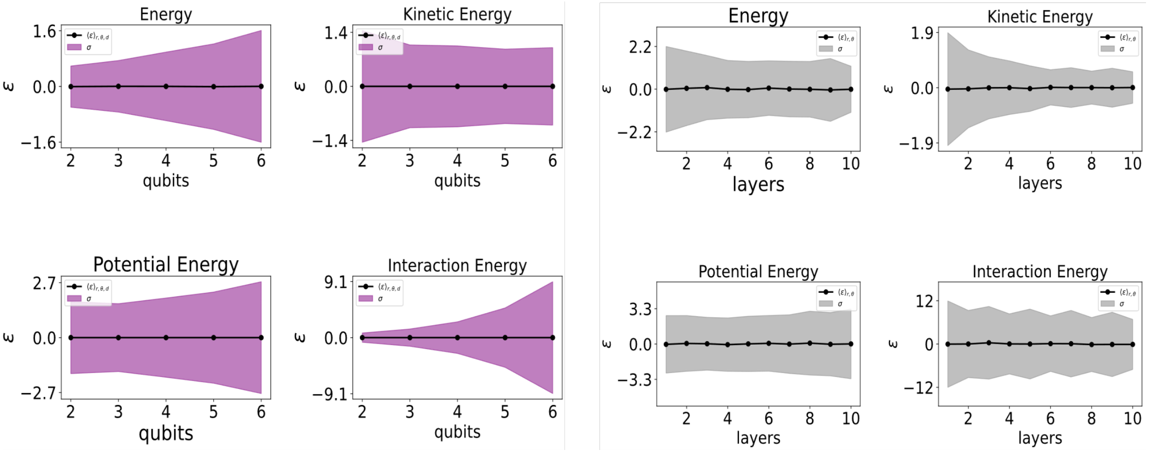

Figure 4: Hadamard test measurement error against system size (left panel) and number of layers in hardware-efficient ansatz (right panel). Parameters are taken as $g = 1, V_0 = 2000$. Each circuit is executed 100 times such that $R = 100$, and one hundred different sets of variational parameters have been considered.

energies, $\langle\langle E\rangle\rangle = \langle\langle E_P\rangle\rangle + \langle\langle E_I\rangle\rangle + \langle\langle E_K\rangle\rangle$, where

$$\begin{aligned} \langle\langle E_P\rangle\rangle &= \sum_{k=0}^{N-1} |\psi_k|^2 V_k \ , \qquad \langle\langle E_I\rangle\rangle = \sum_{k=0}^{N-1} \frac{g}{\delta}|\psi_k|^4 \ , \\ \langle\langle E_K\rangle\rangle &= -\frac{1}{2\delta^2}\sum_{k=0}^{N-1}\left(\psi_k^*\psi_{k+1} - 2\psi_k^*\psi_k + \psi_k^*\psi_{k-1}\right) \ , \end{aligned} \tag{7}$$

for the discretized problem and $\langle\langle\cdots\rangle\rangle$ represent the expectation value [38]. We consider the total energy as the cost function $\mathcal{C} = \sum_j \mathcal{C}_j = \sum_j \langle\langle E_j\rangle\rangle$ for the variational algorithm such that the minimum value of the cost function represents the ground state solution. Figure 3 depicts the quantum circuits to evaluate the kinetic, potential and interaction energies. See arXiv:2403.16426 for more details while the the dataset can be found at DOI 10.25592/uhhfdm.16129.

6.1 Hadamard test measurement error:

Quantum circuits in CQFD often require the measurement of the ancilla qubit alone to extract the value of the cost function through the Hadamard test. The Hadamard test involves measuring the control ancilla qubit in the Pauli-Z basis M times, which enables an estimation of the cost function. However, this approach may result in a larger variance compared to direct measurement methods of the n-qubit quantum register [39]. This variance stems from the Hadamard test outcomes being either +1 or −1, contrasting with direct measurements that yield probability densities across 2^n distinct basis states for more precise cost function estimations. Here, we briefly compare the Hadamard test with direct measurement methods, deferring a detailed analysis to future research.

In order to analyse the error, we consider a fixed Ansatz and random values of variational parameters. For each execution of the quantum circuits, we define the difference of values measured using Hadamard test ($E_i^{Hadamard}$) and direct measurement (E_i^{Direct}) method

$$\Delta E_i = E_i^{Hadamard} - E_i^{Direct}, \tag{8}$$

which allow us to define the average error $\langle\epsilon\rangle_{r,\theta,d}[\langle\epsilon\rangle_{r,\theta}]$ and $\sigma_{r,\theta,d} = \sqrt{\sum[\langle\epsilon\rangle_{r,\theta,d} - \Delta E_i]/\alpha}$ $[\sigma_{r,\theta} = \sqrt{\sum[\langle\epsilon\rangle_{r,\theta} - \Delta E_i]/\alpha}]$ is the standard deviation, where α is the total number of points, r is the number of realization of same quantum circuit, d is the number of layers, and θ represent one random set of variational parameters. Mean value of error and standard deviation highlight an average behaviour of Hadamard test measurement error.

First, we consider varying number of layers from one to ten in hardware-efficient ansatz, $g = 1$, and increase the system size. The left panel of Fig. 4 depicts the mean and standard deviation of error in kinetic, potential, interaction and total energy values. It can be observed that as we increase the system size, spread in total, potential, and interaction energy increase, while there is no clear behaviour of kinetic energy. Second, we fix the system size $N = 2^6$ number of grid points, and increase the number of layers in the ansatz. The right panel of Fig. 4 highlights that there is no clear trend in kinetic, potential, interaction and total energy of the system. This suggests that circuit depth doesn't have significant influence on the Hadamard test measurement error.

6.2 Benchmarking Simulations in Ideal Settings:

We numerically solve NLSE in various parameter regimes characterized by the strength of the nonlinearity. We consider two-local hardware efficient ansatz structure shown in Fig. 3(a). The ansatz structures are constructed for the superconducting devices where only nearest-neighbouring qubits have direct interaction. Due to the absence of any two-qubit gate between distant qubits, these ansatz results in shallower quantum circuits. We employed IBM's QISKIT toolbox to simulate the system on a classical computer. We choose 0.1m shots for each quantum circuit and COBYLA optimizer with fixed number of iterations.

We solve the ground state of the NLSE in week, intermediate and strong regime of nonlinearity for system sizes $n = 2, 3, 4$ and results are presented in Fig. 5(b-f). Difference between variational and exact ground state energy in Fig. 5(b-d) approaches zero in each case, indicating convergence to ground state energy. Below, we focus only on a fixed number of layers to illustrate the performance of the variational algorithm. First, considering a relatively weak nonlinearity strength of $g = 10$, the circular markers in Fig. 5(b) demonstrate the convergence toward the minimum energy, with the energy difference between the variational energy and the ground state energy approaching zero. Second, for intermediate ($g = 500$) and strong ($g = 5000$) nonlinearity strengths, the circular markers in Fig. 5(c) and 5(d) depict the convergence to the minimum energy. The infidelity between the ground and trial state probabilities $F' = \sum_{k=0}^{2^n-1}\left[|\psi_{\mathrm{GS},k}|^2 - |\psi_{\mathrm{var},k}|^2\right]$, indicated by circular markers in Figs. 5(e) and 5(f) for intermediate and strong nonlinearity strengths, respectively, highlights fidelity exceeding 98% upon convergence. This fidelity may substantially improve by initiating the variational algorithm with an educated guess that possesses a considerable overlap with the ground state. These results highlight that the real-amplitude ansatz efficiently approximates the ground state

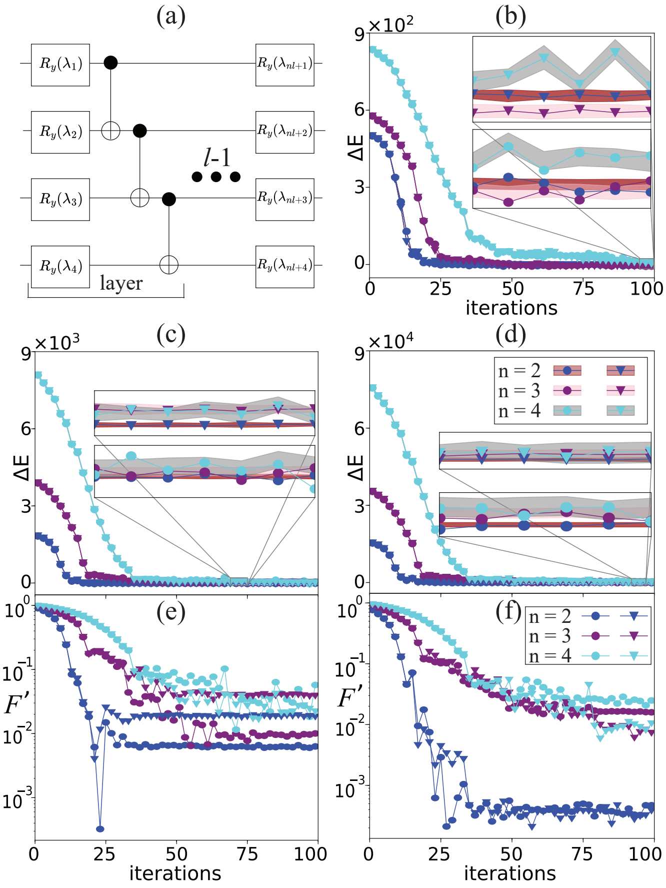

Figure 5: Quantum ansatz (a) and results of noiseless simulations: (b-d) cost function values and (e-f) infidelity between the trial and ground state probabilities. Panel (a) shows the real-amplitude ansatz for the case of $n = 4$, where $R_y(\lambda_i)$ is a parameterized single-qubit rotation gate. Energy difference $\Delta E = \langle\langle E\rangle\rangle_{\mathrm{var}} - \langle\langle E\rangle\rangle_{\mathrm{GS}}$ vs iterations of classical optimizer has been shown for (b) weak nonlinearity $g = 10$, (c) intermediate value of nonlinearity $g = 500$, and (d) strong nonlinearity strength $g = 5000$. Infidelity $F' = \sum_{k=0}^{2^n-1}\left[|\psi_{\mathrm{GS},k}|^2 - |\psi_{\mathrm{var},k}|^2\right]$ is shown in panel (e) and (f) for $g = 500$ and $g = 5000$, respectively. Here, blue, purple, and cyan color indicates the qubit numbers $n = 2$ ($n' = 7$), $n = 3$ ($n' = 10$), and $n = 4$ ($n' = 13$) for $l = 2$, $l = 4$, and $l = 7$ layers, respectively. Moreover, circular and triangular markers indicate 0.1 million and 2 million shots per circuit, respectively, for the cost function evaluation.

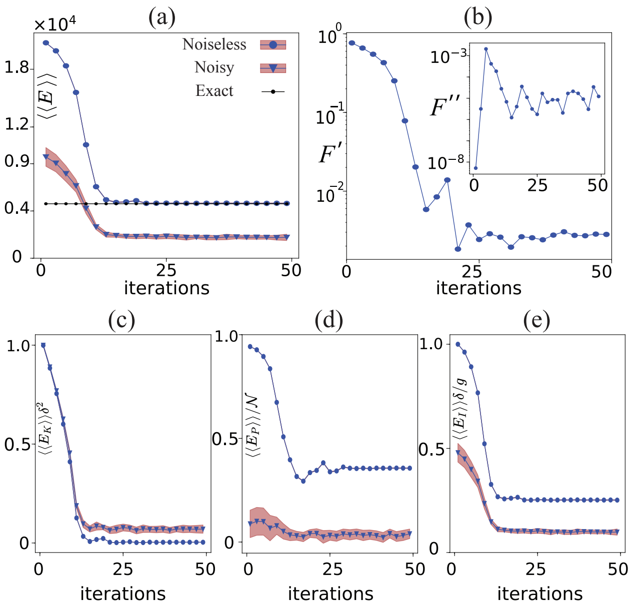

Figure 6: Results for noisy simulations: (a) cost function convergence, (b) infidelity of trial state probabilities, and (c-e) effects of hardware noise on cost function components. Circular (triangular) markers in panel (a) shows the energy $\langle\langle E \rangle\rangle_{\text{var}}$ vs iterations of classical optimizer for $g = 5000$, $n = 2$ ($n' = 7$) and $l = 2$ of real amplitude ansatz in the absence (presence) of quantum noise. Panel (b) (and the inset therein) shows the infidelity $F' = \sum_{k=0}^{2^n-1} \left[|\psi_{\text{GS},k}|^2 - |\psi_{\text{var},k}^{\text{Noisy}}|^2 \right]$ ($F'' = \sum_{k=0}^{2^n-1} \left[|\psi_{\text{var},k}^{\text{Noiseless}}|^2 - |\psi_{\text{var},k}^{\text{Noisy}}|^2 \right]$). Panel (c, d, e) shows the quantities $\langle\langle E_K \rangle\rangle \delta^2$, $\langle\langle E_P \rangle\rangle / \mathcal{N}$, and $\langle\langle E_I \rangle\rangle \delta / g$, which are measured from the ancilla qubit. Here, $\delta = 1/2^n$ and $\mathcal{N}$ is the norm of the potential function.

of the NLSE across different regimes characterized by varying strengths of nonlinearity, thereby demonstrating its expressivity for solving the NLSE with high fidelity. A detailed discussion can be found in arXiv: 2403.16426.

6.3 Simulations Incorporating Superconducting Quantum Hardware Noise

The hardware noise features a mean thermal relaxation time (T_1) of $100\mu s$ and a mean dephasing time (T_2) of $85\mu s$, with standard deviations of $30\mu s$ and $50\mu s$, respectively. It exhibits mean error rates of 2.625×10^{-4} for single-qubit gates and 9.616×10^{-3} for two-qubit gates. Moreover, the mean probability P_{01} (P_{10}) of measuring state $|0\rangle$ ($|1\rangle$) when the qubit is prepared in state $|1\rangle$ ($|0\rangle$) is 2.06×10^{-2} (1.98×10^{-2}). Here, we assume trivial qubit reset noise, ensuring that each qubit is perfectly initialized in the $|0\rangle$ state at the onset of each computation.

Considering n = 2 (n' = 7) qubit system with strong nonlinearity g = 5000, triangular (circular) markers in Fig. 6(a) depict the energy expectation in the presence (absence) of quantum noise. It is important to note that only the energy cost function values obtained in the noisy settings are utilized in the classical optimization to update the variational parameters. Fig. 6(a) highlights that although the energy expectation values from the noisy simulations have smaller magnitudes, they exhibit similar behaviour to those obtained in the noiseless settings. Furthermore, Fig. 6(b) illustrates that the final trial state probabilities in the noisy settings closely matches the ground state, indicating that the noisy simulation converges to the set of variational parameters that approximate the ground state of the problem.

Given the preparation of high-fidelity trial state on the primary quantum register, it is pertinent to consider that quantum noise might influence other distinct processes, such as encoding of the potential function, replication of the variational state, and computation of the energy cost function. To analyze the effect of quantum noise, we examine each component individually, noting the difference in outcomes in the presence and absence of quantum noise. First, we assess the kinetic energy component $\langle\langle E_K \rangle\rangle / \delta^2$, where the corresponding quantum circuit comprises 16 (42) CNOT (single-qubit) quantum gates. As depicted in Fig. 6(c), a minor deviation of approximately 0.05 is observed in kinetic energy values. With the trial state already prepared to high fidelity, the observed discrepancy in kinetic energy values could be attributed to the impact of quantum gate noise during the computation process. Second, we analyze the potential and interaction energy components, $\langle\langle E_P\rangle\rangle/\mathcal{N}$ and $\langle\langle E_I\rangle\rangle\delta/g$, using the corresponding quantum circuits, which incorporate 62 (170) and 133 (273) CNOT (single-qubit) gates, respectively. Notable differences, approximately 0.85 to 0.35 and 0.5 to 0.15 at the initial and final stages of classical optimization, are observed in Figs. 6(d) and 6(e), reflecting the impact of quantum noise. These disparities in potential and interaction energies likely arise from quantum noise affecting the process of encoding the potential function and replicating the trial states on distinct quantum registers, as well as from the bit-wise multiplication across these registers.

Our investigation reveals that deeper quantum circuits with a substantial number of imperfect CNOT and single-qubit gates result in significant deviation and variance in the cost function values, emphasizing the necessity for advanced noise mitigation and/or error correction strategies to improve the quantum computational accuracy and reliability of the variational algorithm.

7 Heat Equation

The Heat or diffusion equation determine the time evolution of a spatial distribution of the temperature field $u(\vec{x},t)$ of a conductive region given an initial temperature distribution $u(\vec{x},0) = u_0$. The data set for gate-based simulation of this equation can be found at the data set at DOI 10.25592/uhhfdm.16108

In one-dimension, the Heat equation reads

$$\frac{\partial u(x,t)}{\partial t} - \kappa \frac{\partial^2 u(x,t)}{\partial x^2} = 0, \quad u(x,0) = u_0, \quad 0 \leq x \leq L, \tag{9}$$

where κ is the thermal diffusivity. As we previously mentioned, we want to write the PDE using second-order finite difference so that we have to discretize the time and the position. Thus in the position x_i at time t_j, the Heat equation reads

$$\frac{u(x_i, t_j + dt) - u(x_i, t_j)}{dt} = \kappa \left[\frac{u(x_i + dx, t_j) - 2u(x_i, t_j) + u(x_i - dx, t_j)}{(dx)^2} \right]. \tag{10}$$

Solving for $u(x_i, t_j + dt)$, we obtain

$$u(x_i, t_{j+1}) = u(x_i, t_j) + \left[\frac{\kappa dt}{(dx)^2} \right] \left[\frac{u(x_{i+1}, t_j) - 2u(x_i, t_j) + u(x_{i-1}, t_j)}{(dx)^2} \right], \tag{11}$$

we have defined $x_{i\pm1} = x_i \pm dx$ that corresponds to the backward/forward difference, similar for the time. The next step is to express Eq. (11) in terms of gates to be implemented on a quantum processor. We should note that the size of spatial discretization of the velocity field corresponds to the size of the multi-qubit i.e, $N_{\max} = 2^n$, where n is the number of two-level system to be used. From Ref [23] we encode the velocity field $u(x,t)$ using the variational circuit depicted in Fig. 2

$$u(x, t_j) = u_j^0 \hat{\mathbf{U}}(\vec{\theta}_j)|\bar{\mathbf{0}}\rangle \tag{12}$$

where u_j^0 is a scaling factor because the wave function is normalized, $|\bar{\mathbf{0}}\rangle$ is a multi-qubit state prepare in their ground state, and $\mathbf{U}(\theta_j)$ is the unitary representing the circuit encoding the field. The selection of $\hat{\mathbf{U}}(\vec{\theta}_j)$ has a deep impact in the convergence of the PDF. The rule of thumb for choosing an adequate anzat is combining shallow circuits that are less prone to be affected by the noise, while be expressive enough to encode all the velocity field but with an optimal number of variational parameters for avoiding *Barren plateaus* [40]. At this stage, we use the hardware efficient ansatz provided by qiskit based on nearest neighbor CNOT gates and controlled-rotations CRY [11], here we choose rotation over the y-axis because we demand real amplitudes for encoding the field $u(x,t)$. We solve iteratively this differential equation by implementing each part of the differential equation on a quantum circuit denoted by $\hat{\mathbf{O}}$, we should note that depending on the PDF the circuit representation of the operator may change. The cost function minimizes the distance between the state after applying $\hat{\mathbf{O}}$ at t_j with the candidate of the solution at t_{j+1}, explicitly

$$C(u_{j+1}^0, \vec{\theta}_j) = ||u(x, t_{j+1}) - (1 + dt)\hat{\mathbf{O}}u(x, t_j)||, \quad \forall j \in (0, N_t) \tag{13}$$

for every time step until N_t. Inspired by the procedure developed in Ref. [23] we write explicitly the cost function in terms of expectation values as follows

$$C(u^0_{j+1},\vec{\theta}_j) = ||u^0_{j+1}|| + ||u^0_j|| - 2u^0_{j+1}u^0_j(E_1+E_2), \tag{14a}$$

$$E_1 = \left[1-2\kappa\frac{dt}{(dx)^2}\right]\langle\bar{\mathbf{0}}|\hat{\mathbf{U}}^\dagger(\vec{\theta}_j)\hat{\mathbf{U}}(\vec{\theta}_{j+1})|\bar{\mathbf{0}}\rangle, \tag{14b}$$

$$E_2 = \kappa\frac{dt}{(dx)^2}\left[\langle\bar{\mathbf{0}}|\hat{\mathbf{U}}^\dagger(\vec{\theta}_j)\hat{\mathbf{A}}\hat{\mathbf{U}}(\vec{\theta}_{j+1})|\bar{\mathbf{0}}\rangle + \langle\bar{\mathbf{0}}|\hat{\mathbf{U}}^\dagger(\vec{\theta}_j)\hat{\mathbf{A}}^\dagger\hat{\mathbf{U}}(\vec{\theta}_{j+1})|\bar{\mathbf{0}}\rangle\right]. \tag{14c}$$

Here, $\hat{\mathbf{A}}$ represents the shifter unitary that shifts the amplitudes of statevector in a periodic way. Therefore, it is straightforward to solve differential equations with periodic boundary conditions by incorporating this shifter unitary into cost function terms. However, for considering problems with Dirichlet boundary conditions, we need to counteract the terms in cost function from periodic shifter. In addition, for Neumann boundary conditions, we need ghost point technique to incorporate information out of boundary into the finite difference method. A way to implement these techniques into the variational quantum algorithm by [24] is proposed by [41] and has been implemented for solved problems in this report, with additional gate-level data sets being available at DOI 10.25592/uhhfdm.14123.

In order to reduce the number of resources used we reduced the number of multi-controlled gates by employing a mathematical trick: any gate whose action on the $|0\rangle^{\otimes n}$ state maps it into itself does not need to be controlled by the measured qubit. Indeed, if we define the gate U where $U|0\rangle^{\otimes n} = |0\rangle^{\otimes n}$, then the action of it's controlled version U_C is the same as the action of the non-controlled version:

$$U_C(|0\rangle+|1\rangle)|0\rangle^{\otimes n} = |0\rangle|0\rangle^{\otimes n} + |1\rangle U|0\rangle^{\otimes n} = |0\rangle U|0\rangle^{\otimes n} + |1\rangle U|0\rangle^{\otimes n} = (|0\rangle+|1\rangle)U|0\rangle^{\otimes n} \tag{15}$$

This defines a wide class of gates, including Toffoli gates and multi controlled Not gates which are a crucial part of the algorithm, thus reducing the number of controlls massively in view with a future experimental demonstration.

7.1 Benchmarking Simulations in Ideal Settings

In this section we run the algorithm in ideal settings. To quantify how good our solutions are, we compute the mean squared error between the classical solution and the obtained with the variational algorithm at time t_j

$$\mathrm{MSE}_j = \frac{1}{N}\sum_i^N [u^{\mathrm{C}}(x_i,t_j) - u^{\mathrm{Q}}(x_i,t_j)]^2 \tag{16}$$

where $u^{\mathrm{C}}(x_i,t_j)$ and $u^{\mathrm{Q}}(x_i,t_j)$ are the classical and quantum solutions, respectively.

For the Heat equation with periodic boundary conditions, we chose the initial condition to be $u(x,0) = \sin(\pi x)$. The equation is solved starting from time $t=0$ to $t=10$ for $n=3,4,5$ qubits. The results for this problem are mentioned in Table 3. A visualization of a result from four qubits ansatz is shown in Figure 7.

N Qubits	dt	Timesteps	N Parameters	Ansatz 2q gates	MSE
3	0.1	100	9	13	1.2e-4
4	0.1	100	16	25	2.2e-4
5	0.01	1000	30	50	23.2e-4
5	0.01	1000	45	77	25.9e-4
5	0.01	1000	55	95	23.2e-4

Table 3: MSE obtained for different number of qubits, after an evolution from $T=0$ to $T=10$

We also solved the heat equation with homogeneous Dirichlet boundary conditions, $u(0,t)=0$ and $u(1,t)=0$. The initial condition for this problem is $u(x,0)=1$. We implemented the ghost point method for treating boundary conditions in variational quantum simulations proposed by [41]. We simulated this problem for $n=3,4$ qubits. The results for this problem are mentioned in Table 4. A visualization of a sample result from three qubits ansatz is shown in Figure 8.

For the next problem, we considered inhomogeneous Dirichlet boundary conditions $u(0,t)=1$ and $u(1,t)=0$. The initial condition for this problem is $u(x,0)=0$. We simulated this problem for $n=3$

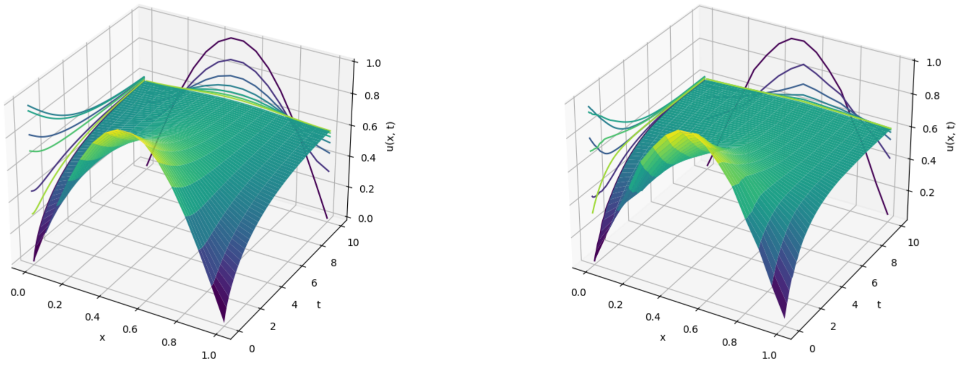

(a) Classical result

(b) Quantum result

Figure 7: Solution of heat equation with periodic boundary conditions using four qubits ansatz. The solution starts at $u(x,0) = \sin(\pi x)$ and ends at $u(x,10) \approx 0$. Additionally, the projection of solution $u(x,t)$ onto planes are represented using lines.

N Qubits	dt	Timesteps	End time	N Parameters	Ansatz 2q gates	MSE
3	1	100	100	12	18	5.9e-7
4	0.1	100	10	20	32	7.8e-7
4	0.1	100	10	24	39	12.2e-7

Table 4: MSE obtained for different number of qubits and timesteps evolution.

qubits. The timestep for this problem is chosen to be 0.1. The problem is solved from $t = 0$ to $t = 10$. The number of parameters for the ansatz is 12. The MSE value of the end timestep is 8.1×10^{-4}. A visualization of a sample result from three qubits ansatz is shown in Figure 9.

These results show excellent agreement between the classical and quantum solutions.

7.2 Benchmarking Simulations with limited statistics

We now perform simulations taking into consideration the probabilistic nature of quantum computers, that is with limited statistics (shot noise). This will be dependent on the number of shots that each architecture allows.

These simulations were performed using $qiskit - Aer$ simulator. We present the results for 3 different shot numbers considered- 1024 shots, 10 000 shots and 100 000 shots. 10 000 shots and 100 000 shots are the maximum possible shot number for Quantinuum's H series and IBM's Sherbrooke, respectively.

Additionally, given that here we are dealing with limited statistics, we present the average MSE score for 10 simulations as well as the standard deviation σ calculated as:

$$\sigma = \sqrt{\frac{\sum_i^{N=10}(MSE_i - \overline{MSE})^2}{N}} \tag{17}$$

For this section we considered the heat equation with periodic boundary conditions and initial conditions: $\kappa = 0.2$ and $u(0,x) = \sin \pi \frac{x}{2^N}^2$. We considered the 3 qubit Hardware Efficient Ansatz with 9 parameters used in the previous section. The results obtained were:

From these results we can clearly see that the number of shots availble will influence the quality of our solution. Indeed, the higher the number of shots, the lower the average mean squared error, $\overline{MSE}$ and the lower the variance, σ. This will motivate to look preferably to platforms that allow a greater number of shots.

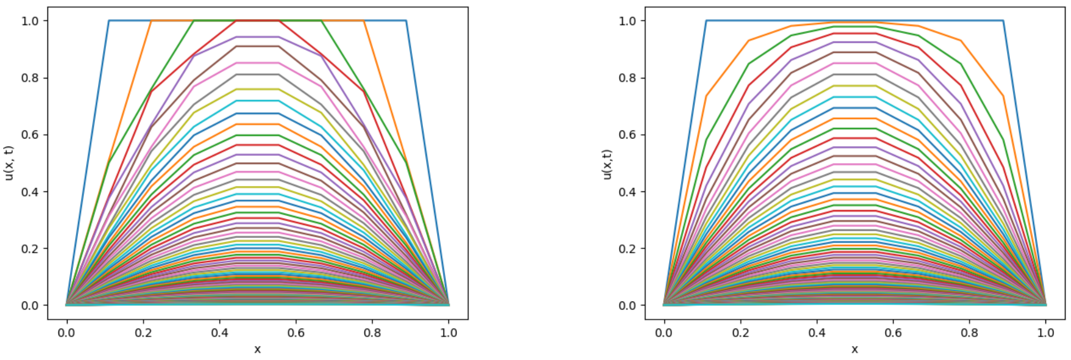

(a) Classical result

(b) Quantum result

Figure 8: Results for heat equation with homogeneous Dirichlet boundary conditions solved using 3 qubits. The solution $u(x,t)$ with homogeneous Dirichlet boundary conditions $u(0,t) = u(1,t) = 0$, initially starts at $u(x,0) = 1$ and ends at $u(x,100) \approx 0$.

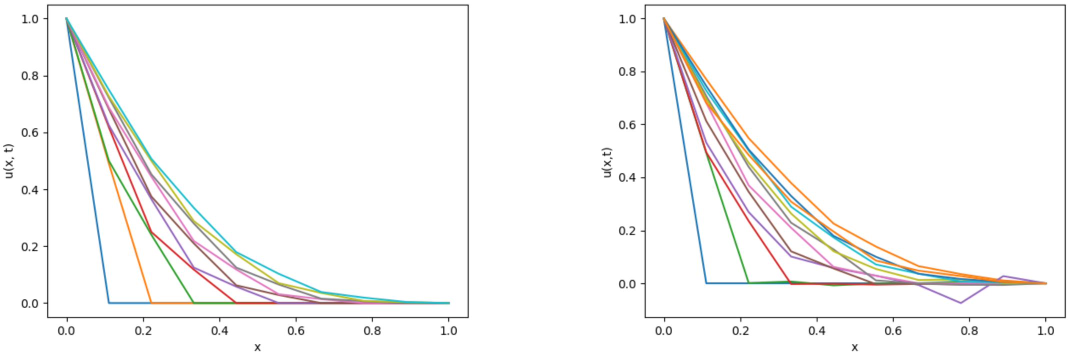

(a) Classical result

(b) Quantum result

Figure 9: Results for heat equation with inhomogeneous Dirichlet boundary conditions solved using 3 qubits. The solution $u(x,t)$ with inhomogeneous Dirichlet boundary conditions $u(0,t) = 1$ and $u(1,t) = 0$, initially starts at $u(x,0) = 0$ and evolved untill $t = 10$.

7.3 Benchmarking Simulations with Noise Models

In this section we performed simulations using noise models based on Hardware. Two models were used, one based on Quantinuum H1 system and one based on IBM Sherbrooke. Whilst the noise model based on IBM Sherbrooke is readily available as part of *qiskit* fake backends, the noise model for Quantinuum H1 was generated using the data available in [1] and qiskit general noise model functions. For both cases, qiskit transpiler was used to convert the circuits into native gates in accordance with the topology of each machine, i.e all to all for quantinuum vs grid based topology for IBM.

Additionally, an error mitigation method, Zero Noise Extrapolation [25], was applied as an error mitigation technique to the IBM simulations. This method improved results substantially. However it cannot be applied to Quantinuum's systems due to the increased cost in computing time and slow measurement characteristic of ion trap computers.

In our case, Zero Noise extrapolation was applied by repeating 2 qubit gates, the biggest source of noise in the current state of the art machines, an odd number of times. The repetition allows us to increase the level of noise present by increasing the number of gates without affecting the ideal evolution of the circuit. Afterwards, by fitting a polynomial, we can estimate the ideal result in the absence of noise. In our case study we performed a quadratic fit by executing every 2 qubit gate 1, 3 and 5 times.

Running the circuits that allow to solve the Heat equation with the same boundary and initial conditions as in the previous section under these noise models we obtain the following results:

From these results we can see the tremendous improvement that Zero Noise Extrapolation has on

Shots	dt	N Timesteps	$\overline{MSE}$	σ
-	0.01	30	0	-
1024	0.01	30	0.055	0.022
10000	0.01	30	0.012	0.004
100000	0.01	30	0.005	0.003

Table 5: Average MSE obtained for different number of shots, evolving from T=0.0 to T=0.3. The first line corresponds to the ideal result

System	dt	Max 2q gate count	ZNE	$\overline{MSE}$	σ
IBM FakeSherbrooke	0.1	90	No	0.602	0.090
IBM FakeSherbrooke	0.1	90	Yes	0.033	0.011
Sim Quantinuum H1	0.1	36	No	0.777	0.391

Table 6: Average MSE obtained under different noise models, evolving from T=0.0 to T=0.3

the IBM simulator. For Quantinuum's systems, we can extract the expected credit cost by using their formula [42]:

$$HQC = 5\frac{N_{1q} + N_{2q} + N_m}{5000} \times S \tag{18}$$

where N_{1q} is the number of single qubit gates, N_{2q} is the number of double qubit gates, N_m is the number of measurements and S is the number of shots.This translates into a cost of 2333 credits for a single call of the loss function for the Hardware Efficient Ansatz and credits for the Symmetry Based Ansatz. Given that $COBYLA$ requires around ≈ 50 calls to converge and the H-series has a computation power of around 1000 credits per hour, this would give a time of 116.65 hours to execute a single time step for the Hardware Efficient Ansatz.

Given these results, an experiment using IBM's hardware appears to be the better solution for a first implementatiomn and will be executed in the following months. Boundary conditions other than periodic conditions result in circuits that are too deep to be run with current processors.

8 Burgers Equation

Moving forwards, we now consider the Burger's equation [43] which is a non-linear PDE that describes the dynamics of a field in presence of diffusion and convection. It is an object of great interest because it is the simplest model where we can observe non-linear effects in fluids such as shockwaves, turbulences and traffic flow due to the competition between diffusion and the non-linear convection. Its one dimensional form reads

$$\frac{\partial f(x,t)}{\partial t} = f(x,t)\frac{\partial f(x,t)}{\partial x} + \nu\frac{\partial^2 f(x,t)}{\partial x^2}, \tag{19}$$

where $f(x,t)$ is the spatiotemporal distribution of the velocity field of the fluid. ν represents the viscosity of the fluid. We solve this equation by again discretizing both position and time. The decomposition of the Laplacian operator is the same as in the Heat equation. Using the finite central difference, we write the convection term as:

$$f(x,t)\frac{\partial f(x,t)}{\partial x} = f(x_i,t_j)\frac{f(x_{i+1},t_j) - f(x_{i-1},t_j)}{2dx}, \tag{20}$$

Here, we propose the same ansatz scheme as in Heat equation

$$f(x,t_j) = \lambda_j^0 U(\vec{\theta}_j)|\mathbf{\bar{0}}\rangle, \tag{21}$$

where again λ_j^0 is a scaling factor due the normalization of the wave function. We use the same cost function as the Heat equation, but the operator $\hat{\mathbf{O}}$ is modified because of the non-linear term. In this case, we can write explicitly the cost function in terms of

$$C(\lambda_{j+1}^0, \vec{\theta}_j) = |\lambda_j^0|^2 + |\lambda_{j+1}^0|^2 - 2\lambda_{j+1}^0\lambda_j^0(E_1 + E_2 + E_3), \tag{22}$$

This project receives funding from the European Union's Horizon 2020 HORIZON Research and Innovation Actions Programme under Grant Agreement #101080085

The second term is the same as in Eq. (14b) and Eq. (14c), and E_3 corresponds to the circuit encoding of the convection part of the Burger's equation:

$$E_3 = \lambda^0_{j+1} \frac{dt}{2dx} \left[\langle \mathbf{\bar{0}} | \mathbf{\hat{U}}^\dagger(\vec{\theta}_j) \mathbf{\tilde{D}}^\dagger \mathbf{A} \mathbf{\hat{U}}(\vec{\theta}_{j+1}) | \mathbf{\bar{0}} \rangle - \langle \mathbf{\bar{0}} | \mathbf{\hat{U}}^\dagger(\vec{\theta}_j) \mathbf{\tilde{D}}^\dagger \mathbf{\hat{A}}^\dagger \mathbf{\hat{U}}(\vec{\theta}_{j+1}) | \mathbf{\bar{0}} \rangle \right]. \tag{23}$$

where the operator $\mathbf{\tilde{D}}$ returns the diagonal field values $f(x_i, t_j)$.

8.1 Benchmarking Simulations in Ideal Settingss

In the master thesis, "Variational quantum algorithms for the 1D Burgers' equation" Greta Reese performed multiple noiseless simulations of the 1D Burgers' equation for different initial conditions and different Ansatze, finding a good agreement between the ideal quantum result and classical simulations [44]. Starting conditions such as delta distributions and triangular distributions were studied and the shuffle anstaz and compact ansatz were used for the execution of the algorithm. Examples of the simulations performed can be seen in figures 10 and 11.

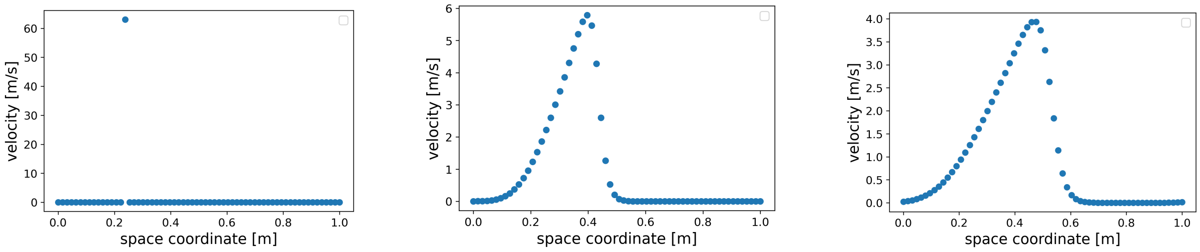

(a) $t = 0$s (b) $t = 2$s (c) $t = 4$s

Figure 10: Classical numerical time evolution of the Burgers' equation for $2^6 = 64$ gridpoints and viscosity $\nu = 0.001 \frac{m^2}{s}$. From the delta velocity distribution at time $t = 0$s, the triangular velocity distribution is formed, which is the theoretical solution for small viscosities $\nu \to 0$. The velocity distribution is moved to the right by the determining advection term.

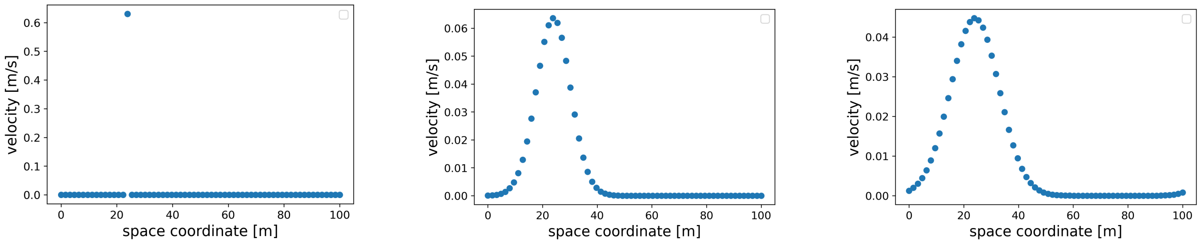

(a) $t = 0$s (b) $t = 2$s (c) $t = 4$s

Figure 11: Classical numerical time evolution of the Burgers' equation for $2^6 = 64$ gridpoints and viscosity $\nu = 10.0 \frac{m^2}{s}$. From the delta velocity distribution at time $t = 0$s, the Gaussian velocity distribution centred on the point of the initial delta distribution is formed, which is the theoretical solution for large viscosities ν.

For more information about these simulations, please refer to Greta Reese's thesis [44], while the data set is available here: DOI https://doi.org/10.25592/uhhfdm.14213.

With the eventual goal of an experimental implementation in the near future that captures non trivial feautures inherent of fluid dynamics, such as a shock-wave we performed further simulations with ansatze more suitable for hardware. We chose as initial condition a sine wave, discretized in 2^n, where n is the number of qubits, along a single dimension. Additionally, we considered periodic boundary conditions, where $f(0) = f(2^n)$ and a viscosity of $\nu = 0.01$.

We also propose a second Ansatz which possesses some additional symmetry information about the solution already defined into its structure - we consider a rotational symmetry around the center point of the field, imposing that the second half of the velocity field has to be the negative of the first. We achieve this by using a Hadamard gate and a Z gate at the last qubit of our ansatz, ensuring that we have a solution of the form $|0\rangle|\psi\rangle^{\otimes n-1} - |1\rangle|\psi\rangle^{\otimes n-1}$ To ensure the correct ordering of the basis state at the second half of the field, we need an additional Toffoli gate to flip the second qubit, a CNOT and 3-controlled-qubit-NOT gate per extra qubit beyond the 3 qubit case. These can be decomposed into Toffolis with the help of additional ancillary qubits. The expected advantage of this Ansatz is that it will converge better to a solution at the expense of being less general. A comparison between the Hardware Efficient Ansatz and the Symmetry Based Ansatz for 3 qubits can be found in figure 12.

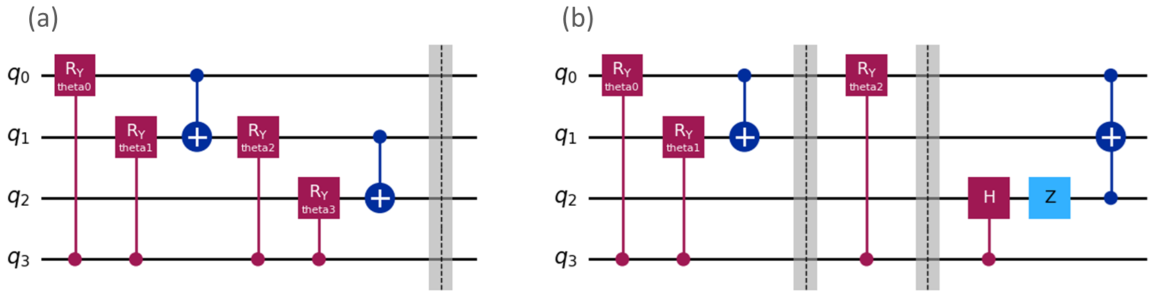

Figure 12: Hardware Efficient Ansatz (a) versus Symmetry Based Ansatz (b), for 3 qubits.

We compare the quantum solution to the classical solution via the MSE just as in the heat equation. To get the classical solution we used the central finite differences for the second derivatives, just as in the quantum method. For the first derivative, the forward difference was used at point 0, the backward difference at point N and the central differences for the inner points. This method showed stability and convergence although more complex methods, such as Runge-Kutta 5 [45] could have been used. We chose the simpler approach for its similarity to the quantum algorithm employed. The quantum solutions were obtained using the BFGS optimizer, directly from the *SciPy* library [46].

Running these Ansatz without noise we obtain the following results:

Ansazt	N Qubits	dt	N 2q gates	N Parameters	MSE
Symmetry Based	3	0.01	11	3	0.001
Hardware Efficient	3	0.01	6	4	0.049
Symmetry Based	4+1	0.01	38	8	0.095
Hardware Efficient	4	0.01	18	12	0.136
Symmetry Based	5+2	0.005	48	106	0.044
Hardware Efficient	5	0.005	60	80	0.000

Table 7: MSE obtained for different Ansatze, after an evolution from $T = 0$ to $T = 0.3$

We present the evolution for the 5 qubit case in figure 13.

For ansatze with more than 4 qubits, a smaller time step of $dt = 0.005$ was necessary for the solution to converge.

From these results we can see that the symmetry ansatz generally takes less parameters and produces lower MSE at the expense of a higher number of 2 qubit gates and required physical qubits for a low amount of qubits (< 5), but this situation reverses for a large amount of qubits. At the same time, for a qubit number ≥ 5, the Hardware Efficient Ansatz produces solutions as good as the results obtained classically. Therefore the Symmetry Based Ansatz will have only a limited utility - it is best suitable for systems that can only handle limited depths, which the current NISQ regime falls into. This motivates the need for simulations with noise to shed a light on how the MSE score is affected by noisy intermediate scale computers.

8.2 Benchmarking Simulations with limited statistics

In this section, we rerun the simulations with limited statistics, and using the same method as in section 7.2 for the cases with 3 and 4 qubits. The results obtained can be found in table 8 and the data set at DOI 10.25592/uhhfdm.16108.

These results were obtained using the *COBYLA* optimizer from the *SciPy* [46] library. This optimizer is more suitable for noisy data, as it is a global optimizer, but it is generally slower than *BFGS*.

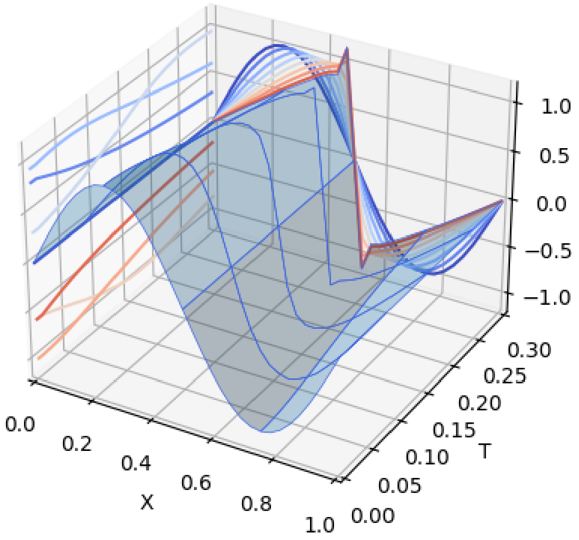

Figure 13: Ideal evolution of the Hardware Ansatz for 5 qubits. A triangular solution is formed, just as expected

Ansazt	N Qubits	dt	$\overline{MSE}$ 1024	σ_{1024}	$\overline{MSE}$ 10k	σ_{10k}	$\overline{MSE}$ 100k	σ_{100k}
Symmetry Based	3	0.01	0.389	0.283	0.116	0.031	0.074	0.023
Hardware Efficient	3	0.01	0.387	0.297	0.1656	0.032	0.106	0.017
Symmetry Based	4+1	0.01	0.765	0.270	0.178	0.035	0.170	0.077
Hardware Efficient	4	0.01	1.061	0.733	0.508	0.119	0.354	0.076

Table 8: MSE obtained for different Ansatze, after an evolution from $T = 0$ to $T = 0.3$ with limited statistics

From these results we can already see that the number of shots used is crucial for an actual implementation. Indeed, the results with just 1024 shots produced a much higher MSE.

This motivates us to look preferably to solid state platforms, such as superconducting qubits, due to their higher number of available shots and to investigate further into variance reduction methods, such as the ones presented in [39, 47] which could be crucial for experimental implementations.

8.3 Benchmarking Simulations with Noise Model Statistics

Due to the depth and number of expectation values required to solve the Burgers equation, in this section we only performed the simulations with 3 problem qubits given that circuits beyond these sizes will mainly result in random noise. Additionally, we considered 2 different time steps, $dt = 0.1$ and $dt = 0.3$. We increased the time step to reflect the limited computing time available on these machines.

Again, due to limited statistics and the stochastic nature of the noise studied, we present an average MSE score over 5 different runs. For IBM's noise model, we present the result with and without Zero Noise Extrapolation.

The simulations using Quantinuum's noise model were obtained assuming 10 thousands shots whilst the ones performed with IBM's noise assume 100 thousand shots. The obtained results are presented in table 9 and the data set at DOI 10.25592/uhhfdm.16108.

From these results we can see that Quantinuum's system, as expected due to their lower errors, produces better results, although their variance is slightly higher given the lower shot count. At the same time, we can also see that Zero Noise Extrapolation generally improved the simulated results, at

This project receives funding from the European Union's Horizon 2020 HORIZON Research and Innovation Actions Programme under Grant Agreement #101080085

Ansatz	N Qubits	dt	System	ZNE	Max 2Q gates	$\overline{MSE}$	σ
Symmetry Based	8	0.1	Sim Quantinuum H1	No	46	0.159	0.027
Symmetry Based	8	0.1	IBM FakeSherbrooke	No	133	0.432	0.034
Symmetry Based	8	0.1	IBM FakeSherbrooke	Yes	133	0.256	0.090
Hardware Efficient	8	0.1	Sim Quantinuum H1	No	31	0.175	0.041
Hardware Efficient	8	0.1	IBM FakeSherbrooke	No	91	0.226	0.039
Hardware Efficient	8	0.1	IBM FakeSherbrooke	Yes	91	0.117	0.013
Symmetry Based	8	0.3	Sim Quantinuum H1	No	46	0.097	0.047
Symmetry Based	8	0.3	IBM FakeSherbrooke	No	133	0.478	0.032
Symmetry Based	8	0.3	IBM FakeSherbrooke	Yes	133	0.186	0.065
Hardware Efficient	8	0.3	Sim Quantinuum H1	No	31	0.108	0.020
Hardware Efficient	8	0.3	IBM FakeSherbrooke	No	91	0.136	0.016
Hardware Efficient	8	0.3	IBM FakeSherbrooke	Yes	91	0.138	0.088

Table 9: MSE score for 3 qubits, under expected noisy conditions for IBM's sherbrooke and Quantinuum's H1

the expense of a higher variance, just as expected.

Again, for Quantinuum's systems, we can extract the expected credit cost by using their formula [42]:

$$HQC = 5\frac{N_{1q} + N_{2q} + N_m}{5000} \times S \tag{24}$$

where N_{1q} is the number of single qubit gates, N_{2q} is the number of double qubit gates, N_m is the number of measurements and S is the number of shots. This translates into a cost of 2093 credits for a single call of the loss function for the Hardware Efficient Ansatz and 4387 credits for the Symmetry Based Ansatz. Given that $COBYLA$ requires around $\approx$ 50 calls to converge and the H-series has a computation power of around 1000 credits per hour, this would give a time of 145.15 hours to execute a single time step for the Hardware Efficient Ansatz and 219.35 for the Symmetry Based Ansatz.

These time frames are completely infeasible. Unfortunately there is no easy fix here. We could potentially reduce the number of shots, which could vastly reduce the number of credits consume but as seen in section 7.2 this would lead to a large increase in error. Additional optimization of the circuits could reduce the number of single and double qubit gates, but given the reduced size of the Ansatze here considered, this is not obvious. Another avenue would be to take a different optimizer that does not require as many calls to converge, but so far no such optimizer was found. Therefore, at the moment, it seems apparent the need to use superconducting qubits for experimental implementations of this algorithm, given their faster gate and measurement speed necessary for the cumbersome optimization.

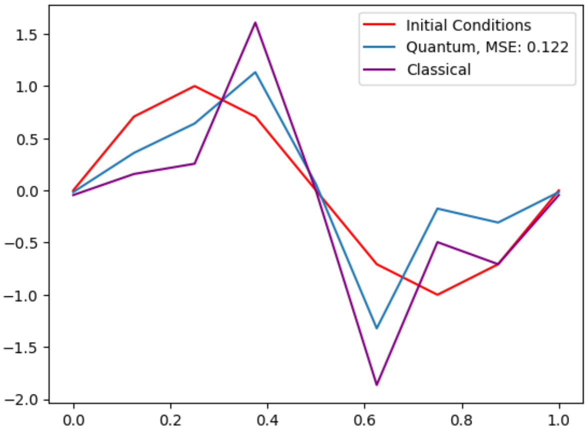

Figure 14: Velocity field simulated with Fake Sherbrooke for a single time step of 0.3. A shock wave is clearly emerging in the quantum solution. This run finished with an MSE of 0.122.

At the same time, we also see that the time discretization is not a dominant factor for the MSE obtained, so an implementation with a single time step, instead of iteration seems reasonable for the current NISQ era.

That said, the solutions obtained simulating IBM's Fake Sherbrooke can be clearly improved. Possible paths forward would be to implement better noise mitigation and use better quantum chips. Nonetheless we can clearly see the emergence of non trivial features, such as a shock wave, on our simulated solutions, as as shown in figure 14. This demonstrates that Quantum Computers are well positioned for the study of features that are hard to classically simulate, such as shock waves and turbulence.

References

[1] Lawrence C Evans. *Partial differential equations*, volume 19. American Mathematical Society, 2022.

[2] Gordon D Smith. *Numerical solution of partial differential equations: finite difference methods.* Oxford university press, 1985.

[3] Frank Arute, Kunal Arya, Ryan Babbush, Dave Bacon, Joseph C. Bardin, Rami Barends, Rupak Biswas, Sergio Boixo, Fernando G. S. L. Brandao, David A. Buell, Brian Burkett, Yu Chen, Zijun Chen, Ben Chiaro, Roberto Collins, William Courtney, Andrew Dunsworth, Edward Farhi, Brooks Foxen, Austin Fowler, Craig Gidney, Marissa Giustina, Rob Graff, Keith Guerin, Steve Habegger, Matthew P. Harrigan, Michael J. Hartmann, Alan Ho, Markus Hoffmann, Trent Huang, Travis S. Humble, Sergei V. Isakov, Evan Jeffrey, Zhang Jiang, Dvir Kafri, Kostyantyn Kechedzhi, Julian Kelly, Paul V. Klimov, Sergey Knysh, Alexander Korotkov, Fedor Kostritsa, David Landhuis, Mike Lindmark, Erik Lucero, Dmitry Lyakh, Salvatore Mandrà, Jarrod R. McClean, Matthew McEwen, Anthony Megrant, Xiao Mi, Kristel Michielsen, Masoud Mohseni, Josh Mutus, Ofer Naaman, Matthew Neeley, Charles Neill, Murphy Yuezhen Niu, Eric Ostby, Andre Petukhov, John C. Platt, Chris Quintana, Eleanor G. Rieffel, Pedram Roushan, Nicholas C. Rubin, Daniel Sank, Kevin J. Satzinger, Vadim Smelyanskiy, Kevin J. Sung, Matthew D. Trevithick, Amit Vainsencher, Benjamin Villalonga, Theodore White, Z. Jamie Yao, Ping Yeh, Adam Zalcman, Hartmut Neven, and John M. Martinis. Quantum supremacy using a programmable superconducting processor. *Nature*, 574(7779):505–510, Oct 2019.

[4] Lov K. Grover. Quantum computers can search arbitrarily large databases by a single query. *Phys. Rev. Lett.*, 79:4709–4712, Dec 1997.

[5] M. Cerezo, Andrew Arrasmith, Ryan Babbush, Simon C. Benjamin, Suguru Endo, Keisuke Fujii, Jarrod R. McClean, Kosuke Mitarai, Xiao Yuan, Lukasz Cincio, and Patrick J. Coles. Variational quantum algorithms. *Nature Reviews Physics*, 3(9):625–644, Sep 2021.

[6] John Preskill. Quantum computing in the nisq era and beyond. *Quantum*, 2:79, 2018.

[7] Lars S. Madsen, Fabian Laudenbach, Mohsen Falamarzi. Askarani, Fabien Rortais, Trevor Vincent, Jacob F. F. Bulmer, Filippo M. Miatto, Leonhard Neuhaus, Lukas G. Helt, Matthew J. Collins, Adriana E. Lita, Thomas Gerrits, Sae Woo Nam, Varun D. Vaidya, Matteo Menotti, Ish Dhand, Zachary Vernon, Nicolás Quesada, and Jonathan Lavoie. Quantum computational advantage with a programmable photonic processor. *Nature*, 606(7912):75–81, Jun 2022.

[8] QuEra Computing. Aquila, our 256-qubit quantum processor. `https://www.quera.com/aquila`, May 2023. Accessed: 2023-05-23.

[9] Colin D Bruzewicz, John Chiaverini, Robert McConnell, and Jeremy M Sage. Trapped-ion quantum computing: Progress and challenges. *Applied Physics Reviews*, 6(2), 2019.

[10] Rigetti Computing. Rigetti computing, 2024. Accessed: 2024-09-25.

[11] Ali Javadi-Abhari, Matthew Treinish, Kevin Krsulich, Christopher J. Wood, Jake Lishman, Julien Gacon, Simon Martiel, Paul D. Nation, Lev S. Bishop, Andrew W. Cross, Blake R. Johnson, and Jay M. Gambetta. Quantum computing with Qiskit, 2024.

[12] J. M. Pino, J. M. Dreiling, C. Figgatt, J. P. Gaebler, S. A. Moses, M. S. Allman, C. H. Baldwin, M. Foss-Feig, D. Hayes, K. Mayer, C. Ryan-Anderson, and B. Neyenhuis. Demonstration of the trapped-ion quantum ccd computer architecture. *Nature*, 592(7853):209–213, Apr 2021.

[13] Steve Olmschenk, Kelly C Younge, David L Moehring, Dzmitry N Matsukevich, Peter Maunz, and Christopher Monroe. Manipulation and detection of a trapped yb+ hyperfine qubit. *Physical Review A—Atomic, Molecular, and Optical Physics*, 76(5):052314, 2007.

[14] Klaus Mølmer and Anders Sørensen. Multiparticle entanglement of hot trapped ions. *Phys. Rev. Lett.*, 82:1835–1838, Mar 1999.

[15] J. P. Gaebler, C. H. Baldwin, S. A. Moses, J. M. Dreiling, C. Figgatt, M. Foss-Feig, D. Hayes, and J. M. Pino. Suppression of midcircuit measurement crosstalk errors with micromotion. *Phys. Rev. A*, 104:062440, Dec 2021.

[16] Jens Koch, Terri M. Yu, Jay Gambetta, A. A. Houck, D. I. Schuster, J. Majer, Alexandre Blais, M. H. Devoret, S. M. Girvin, and R. J. Schoelkopf. Charge-insensitive qubit design derived from the cooper pair box. *Phys. Rev. A*, 76:042319, Oct 2007.

[17] V. Bouchiat, D. Vion, P. Joyez, D. Esteve, and M. H. Devoret. Quantum coherence of charge states in the single electron box. *Journal of Superconductivity*, 12(6):789–797, Dec 1999.

[18] G. S. Paraoanu. Microwave-induced coupling of superconducting qubits. *Phys. Rev. B*, 74:140504, Oct 2006.

[19] Chad Rigetti and Michel Devoret. Fully microwave-tunable universal gates in superconducting qubits with linear couplings and fixed transition frequencies. *Phys. Rev. B*, 81:134507, Apr 2010.

[20] A. Wallraff, D. I. Schuster, A. Blais, L. Frunzio, J. Majer, M. H. Devoret, S. M. Girvin, and R. J. Schoelkopf. Approaching unit visibility for control of a superconducting qubit with dispersive readout. *Phys. Rev. Lett.*, 95:060501, Aug 2005.

[21] D. I. Schuster, A. Wallraff, A. Blais, L. Frunzio, R.-S. Huang, J. Majer, S. M. Girvin, and R. J. Schoelkopf. ac stark shift and dephasing of a superconducting qubit strongly coupled to a cavity field. *Phys. Rev. Lett.*, 94:123602, Mar 2005.

[22] P. Krantz, M. Kjaergaard, F. Yan, T. P. Orlando, S. Gustavsson, and W. D. Oliver. A quantum engineer's guide to superconducting qubits. *Applied Physics Reviews*, 6(2):021318, 06 2019.

[23] Michael Lubasch, Jaewoo Joo, Pierre Moinier, Martin Kiffner, and Dieter Jaksch. Variational quantum algorithms for nonlinear problems. *Phys. Rev. A*, 101:010301, Jan 2020.

[24] Michael Lubasch, Jaewoo Joo, Pierre Moinier, Martin Kiffner, and Dieter Jaksch. Variational quantum algorithms for nonlinear problems. *Physical Review A*, 101(1):010301, 2020.

[25] Abhinav Kandala, Kristan Temme, Antonio D. Córcoles, Antonio Mezzacapo, Jerry M. Chow, and Jay M. Gambetta. Error mitigation extends the computational reach of a noisy quantum processor. *Nature*, 567(7749):491–495, Mar 2019.

[26] A. Scott. *Encyclopedia of nonlinear science*. Routledge, New York, 2006.

[27] G. Agrawal. *Nonlinear fiber optics*. 2013.

[28] K. Nakkeeran. Nonlinear waves in atomic media. *Chaos, Solitons & Fractals*, 13:673, 2002.

[29] H. Triki, C. Bensalem, A. Biswas, S. Khan, Q. Zhou, S. Adesanya, S. P. Moshokoa, and M. Belic. Nonlinear optical phenomena. *Optics Communications*, 437:392, 2019.

[30] C. Sulem and P.-L. Sulem. *The nonlinear Schrödinger equation: self-focusing and wave collapse*. Springer Science & Business Media, 1999.

[31] E. P. Gross. Structure of a quantized liquid. *Il Nuovo Cimento (1955-1965)*, 20:454, 1961.

[32] L. P. Pitaevskii. Vortex lines in superfluid he ii. *Sov. Phys. JETP*, 13:451, 1961.

[33] F. Dalfovo, S. Giorgini, L. P. Pitaevskii, and S. Stringari. Theory of bose-einstein condensation in trapped gases. *Reviews of Modern Physics*, 71:463, 1999.

[34] A. J. Leggett. Bose-einstein condensation in the alkali gases: a status report. *Reviews of Modern Physics*, 73:307, 2001.

[35] L. Pitaevskii and S. Stringari. *Bose-Einstein condensation*. 2003.

[36] M. Edwards and K. Burnett. Quantum dynamics of trapped bose gases. *Physical Review A*, 51:1382, 1995.

[37]

[38] M. Lubasch, J. Joo, P. Moinier, M. Kiffner, and D. Jaksch. Nonlinear dynamics of light in multimode systems. *Physical Review A*, 101:010301, 2020.

[39] Stefano Polla, Gian-Luca R Anselmetti, and Thomas E O'Brien. Optimizing the information extracted by a single qubit measurement. *Physical Review A*, 108(1):012403, 2023.

[40] Martin Larocca, Supanut Thanasilp, Samson Wang, Kunal Sharma, Jacob Biamonte, Patrick J Coles, Lukasz Cincio, Jarrod R McClean, Zoë Holmes, and M Cerezo. A review of barren plateaus in variational quantum computing. *arXiv preprint arXiv:2405.00781*, 2024.

[41] Paul Over, Sergio Bengoechea, Thomas Rung, Francesco Clerici, Leonardo Scandurra, Eugene de Villiers, and Dieter Jaksch. Boundary treatment for variational quantum simulations of partial differential equations on quantum computers. *arXiv preprint arXiv:2402.18619*, 2024.

[42] Quantinuum H1 series model, published = https://www.quantinuum.com/products-solutions/system-model-h1-series. Accessed: 2024-10-10.

[43] Mayur P Bonkile, Ashish Awasthi, C Lakshmi, Vijitha Mukundan, and VS Aswin. A systematic literature review of burgers' equation with recent advances. *Pramana*, 90:1–21, 2018.

[44] Greta Reese. Variational quantum algorithms for the 1d burgers' equation. Master's thesis, University of Hamburg, 2022.

[45] John Charles Butcher. A history of runge-kutta methods. *Applied numerical mathematics*, 20(3):247–260, 1996.

[46] Pauli Virtanen, Ralf Gommers, Travis E. Oliphant, Matt Haberland, Tyler Reddy, David Cournapeau, Evgeni Burovski, Pearu Peterson, Warren Weckesser, Jonathan Bright, Stéfan J. van der Walt, Matthew Brett, Joshua Wilson, K. Jarrod Millman, Nikolay Mayorov, Andrew R. J. Nelson, Eric Jones, Robert Kern, Eric Larson, C J Carey, İlhan Polat, Yu Feng, Eric W. Moore, Jake VanderPlas, Denis Laxalde, Josef Perktold, Robert Cimrman, Ian Henriksen, E. A. Quintero, Charles R. Harris, Anne M. Archibald, Antônio H. Ribeiro, Fabian Pedregosa, Paul van Mulbregt, and SciPy 1.0 Contributors. SciPy 1.0: Fundamental Algorithms for Scientific Computing in Python. *Nature Methods*, 17:261–272, 2020.

[47] Thomas E O'Brien, Stefano Polla, Nicholas C Rubin, William J Huggins, Sam McArdle, Sergio Boixo, Jarrod R McClean, and Ryan Babbush. Error mitigation via verified phase estimation. *PRX Quantum*, 2(2):020317, 2021.